Catalysis Today 284 (2017) 146–152

Contents lists available at ScienceDirect

Catalysis Today

journal homepage: www.elsevier.com/locate/cattod

Competitive ion-exchange of manganese and gadolinium in titanate nanotubes

Péter Szirmai [1], Jeremy Stevens [1], Endre Horváth *, Luka Ćirić, Márton Kollár, László Forró, Bálint Náfrádi *

Laboratory of Physics of Complex Matter, Ecole Polytechnique Fédérale de Lausanne, Station 3, CH-1015 Lausanne, Switzerland

ARTICLE INFO

Article history:
Received 14 July 2016
Received in revised form 9 October 2016
Accepted 6 November 2016
Available online 26 November 2016

Keywords:
Co-doping
Ion-exchange
Manganese
Gadolinium
Zero-field splitting
ESR

ABSTRACT

Homogeneous Mn^{2+} and Gd^{3+} intercalation of scroll-type trititanate nanotubes using a post-synthesis ion exchange method is reported. Compared to Mn^{2+}, Gd^{3+} ion-exchange shows larger saturation intercalation levels. Upon co-doping, weak interactions between the dopant ions were found to modify the incorporated concentrations. Electron spin resonance (ESR) measurements, performed at several frequencies, confirmed the homogeneous distribution of Mn^{2+} and Gd^{3+}. Detailed simulation of ESR spectra identified a large spread of the local structural distortions of the occupied sites as a result of a wide range of curvature radii of the titanate nanotubes.

1. Introduction

The wide range of applications of titanium dioxide (TiO_2) and its biocompatibility made it the most studied oxide material in the last 30 years [1,2]. Apart from its classic use as a pigment, it turned out to enhance the efficiency of dye-sensitized solar cells (DSSCs) [3], it possesses unique photocatalytic activity [4–7], and it is the central component of the hole blocking layer in perovskite solar cells [8–10]. In addition, it is widely used in sensors [11,12], memristors [13], supercapacitors [14,15] and batteries [16]. Furthermore, the one-dimensional titanium dioxide nanotubes outperform their bulk counterpart in Grätzel-type solar cells and in photocatalytic applications, and have stimulated significant research interest since their discovery [17]. In contrast to TiO_2 nanoparticles, the rolled-up titanate nanotubes have a larger surface area [18,19] and the one-dimensionality in sintered systems leads to longer electron diffusion lengths in DSSCs [20]. Compared to the Degussa P25 reference material [21], i.e. nanoparticles that are mixtures of rutile and anatase, enhanced photocatalytic activity was found in these titania nanotubes. Notably, this photoactivity turned out to depend heavily on the morphology, diameter, and annealing methods [22–24].

One of the major disadvantages of TiO_2 in photocatalytic applications remains, however, its large band gap of 3.2 eV giving an absorption of only about 3–5% in the solar spectrum. Doping of titanate nanotubes with metal and nonmetal ions [25], or co-doping it with Gd^{3+} and nitrogen [26] were found to increase the photocatalytic activity up to a certain threshold. As well, doping of TiO_2 nanotubes leads to an increase in surface area due to the decreased particle size, dopant ions may become charge trap sites, and may act as photosensitizers [26,27,28,29]. Furthermore, in electronic and optoelectronic applications, the band gap tunability and the ability to induce impurity levels would be highly desirable. In particular, nanotubes prepared by a hydrothermal technique [30] can be easily doped using predoped TiO_2 particles [31], doping during the hydrothermal growth [32], or using post-synthesis ion-exchange [33].

As the intercalation takes place in the titanate phase in several cases [27–29], it is of great importance to provide information about the ion-exchange positions of the intercalated titanates. Nevertheless, it is subject to controversy [33] as to whether these synthesis routes lead to homogeneous doping of the titanate nanotubes or whether, after calcination, they result in doped TiO_2 nanotubes with superior photocatalytic activity. Several reports confirmed that the observed advantageous properties of titanate nanotubes upon intercalation might arise from the presence of dopant aggre-

* Corresponding authors.
E-mail addresses: endre.horvath@epfl.ch (E. Horváth), nafradi@yahoo.com (B. Náfrádi).
[1] Equally contributing (first) authors.

http://dx.doi.org/10.1016/j.cattod.2016.11.010
0920-5861/

gates [34,35]. Furthermore, comparison of the different synthesis methods and their future scale-up is difficult as only the nominal concentrations are known and the incorporated concentrations may differ. In the case of co-doping with different dopant ions, the ion-exchange efficiencies may be correlated and interactions between dopant ions may result in the formation of aggregates. Whereas high-resolution transmission electron microscopy can identify the local distribution of dopants in a small number of nanotubes, microscopic local probes, such as the electron spin resonance (ESR) technique has the advantage to confirm homogeneity and ion-exchange efficiency, as well as for the selective identification of dopant ions in larger sample sizes. To extend our previous study [33], where Mn^{2+} was used as a dopant, here, we used Gd^{3+} as co-dopant, which is a well-established local probe in ESR studies [36,37] and has a higher oxidation state.

Here, we report the low-temperature synthesis of Mn^{2+} and Gd^{3+} co-doped trititanate nanotubes using a post-synthesis ion exchange route. As reported earlier [33], our synthesis method results in homogeneous intercalation of the co-dopants. Co-doping is studied by energy-dispersive X-ray spectroscopy (EDX), X-ray fluorescence (XRF), and ESR spectroscopies. We focus on the ion-exchange competition between the two different metal ions with different oxidation states. We determine the ion-exchange capacities both for Gd^{3+} and for Mn^{2+}. Our multi-frequency ESR study along with detailed numerical simulation of zero-field splitting tensor reveals the spatial selectivity and precise distribution of Gd^{3+} ions in trititanate nanotubes.

2. Experimental methods

Titanate nanotubes ($H_2Ti_3O_7$) were synthesized following the method developed in Ref. [33]. During the synthesis process Na^+ ions were exchanged with H^+ by neutralizing the water solution of $Na_2Ti_3O_7$ until obtaining a pH ≈ 6.5, as confirmed by the EDX and XRF measurements.

To perform the ion-exchange and study the competition of Mn^{2+} and Gd^{3+}, two alternative procedures were used. In both cases, $Mn(NO_3)_2 \times H_2O$ (Aldrich, 99.99%) and $Gd(CH_3CO_2)_3 \times H_2O$ (Aldrich, 99.9%) were the source of Mn^{2+} and Gd^{3+} ions. As the surface potential of the titanate nanotubes remains negative even for moderately acidic solutions [38], we speculate that the choice of the anions does not affect the resulting ion-exchange efficiencies. Thus, only the metal cations are believed to play a role in setting the intercalation levels.

Upon storage, precipitation of Gd^{3+} and Mn^{2+} ions has been observed in distilled water solutions. Therefore, all the ion-exchange reactions were performed with freshly prepared salt solutions.

In the first synthesis method, 5 ml of the $H_2Ti_3O_7$ suspension (with 100 g/l trititanate nanotube dispersed in distilled water) and respective amounts of distilled water solutions of $Mn(NO_3)_2 \times H_2O$ (5.6 g/l with respect to Mn^{2+} content) or $Gd(CH_3CO_2)_3 \times H_2O$ (8.7 g/l with respect to Gd^{3+} content) were mixed for 1 h at room temperature. Note that during this process the pH was always kept below pH ≈ 9.

This method was used for the preparation of three samples (Mn-1, Mn-Gd-1, and Gd-1 samples, see Table 1). To further examine the competition between Mn^{2+} and Gd^{3+}, the distilled water solution of $Gd(CH_3CO_2)_3 \times H_2O$ was introduced 20 min later than the distilled water solution of $Mn(NO_3)_2 \times H_2O$ in the case of the equally intercalated sample (Mn-Gd-1).

As an alternative synthesis method, $Mn(NO_3)_2 \times H_2O$ and $Gd(CH_3CO_2)_3 \times H_2O$ salts were dissolved in 5 ml of the $H_2Ti_3O_7$ suspension while stirring the suspension. For all three samples (Gd-2, Mn-Gd-2, and Gd-3, see Table 1), the intercalation took place for 1 h at room temperature.

The suspension is subsequently filtered and washed with 500 ml of deionized water in order to remove the non-exchanged Mn^{2+} and Gd^{3+} remaining in the solution. Then we dried the samples at 130 °C. Whereas titanate nanotubes are not stable in strongly acidic solutions [39], the dried powder samples are stable under ambient conditions.

For the ESR measurements at 9.4 GHz we used a commercial Bruker ELEXSYS X-Band spectrometer at room temperature for which the maximum magnetic field stands at 1.5 T. For higher frequency ESR (52, 78, 105, 157, 210, 315 and 420 GHz) we used a home-built spectrometer whose specifications are given in Refs. [40,41]. We used Mn:MgO with a known (1.5 ppm) Mn^{2+} concentration in X-band ESR as a *g*-factor and intensity standard. The absolute spin-susceptibility was calculated as described elsewhere [42].

Scanning electron microscope (SEM) images were taken with a MERLIN Zeiss electron microscope. The atomic concentrations of gadolinium and manganese were determined by energy-dispersive X-ray spectroscopy (EDX).

Transmission electron microscope (TEM) and scanning transmission electron microscope (STEM) images were taken with a FEI Titan Themis microscope.

X-Ray Fluorescence spectrometry was performed with an Orbis PC Micro EDXRF analyser. Gadolinium ESR spectra were simulated using the simulation software Easyspin, which allows us to simulate spectra and fit ESR data [43]. Simulation parameters include the *g*-factor and zero-field splitting *D* and *E*, which we retrieved from the literature [44,45]. To simulate the broadening of our spectrum, Gaussian distributions of *D* and *E* values are defined. We also included an intrinsic peak to peak linewidth broadening via the convolution of the calculated spectrum with a derivative Lorentzian function of peak to peak linewidth ΔB_{int}. This intrinsic linewidth indicates that there exists a residual, field-independent linewidth. This is expected in the case of gadolinium because of the non-negligible spin-orbit interaction.

3. Results and discussion

3.1. EDX and XRF measurements

Six samples with different dopant concentrations were compared in our study. As shown in Fig. 1a, the typical SEM image proves that scroll-type trititanate nanotubes are produced with a prevailing tubular morphology (Fig. 1b-c) of the doped material. As shown in our previous study [33], ion-exchange positions are well-defined in rolled-up trititanate nanotubes (see Fig. 1d-e). A summary of their nominal and incorporated compositions determined by EDX, XRF, and ESR measurements is given in Table 1.

As seen in Table 1, the measured incorporated concentrations show a significant scattering for the three different experimental techniques. This discrepancy is all the more obvious at low concentrations, indicating that it might not stem from the inhomogeneous intercalation but it is due to intrinsic instrumental detection limits of EDX and XRF.

As ESR is a bulk-sensitive method, whereas both EDX and XRF are surface-sensitive techniques, the combination of the three spectroscopic techniques provides evidence of homogeneous doping in our samples. Unlike EDX and XRF, ESR is sensitive to the oxidation state, thus the oxidation states in our samples are only Mn^{2+} and Gd^{3+} states (see below).

Samples Mn-1, Mn-Gd-1, and Gd-1 were prepared by mixing a $H_2Ti_3O_7$ nanotube suspension with a distilled water solution of known concentration (see the Experimental Methods) of $Mn(NO_3)_2 \times H_2O$ and $Gd(CH_3CO_2)_3 \times H_2O$ salts, whereas samples

Table 1
Elemental compositions of the six samples. Nominal and incorporated atomic concentrations are given with respect to titanium atoms. The doping efficiencies are calculated by dividing the incorporated atomic concentrations by the nominal atomic concentrations. Note that the X-band ESR spectra of Mn^{2+} and Gd^{3+} overlap, which prevents the calculation of the efficiencies for the co-doped samples.

		EDX		XRF		ESR	
Sample	Nominal at.%	Incorporated at.%	Ion-exchange Efficiency[a]	Incorporated at.%	Ion-exchange Efficiency[a]	Incorporated at.%	Ion-exchange Efficiency[a]
Mn-1	1.7% Mn	0.22% Mn	0.13 Mn	0.16% Mn	0.09 Mn	0.64% Mn	0.37 Mn^{2+}
Mn-	3.1% Mn	0.2% Mn	0.06 Mn	0.83% Mn	0.27 Mn		
Gd-	3.1% Gd	1.7% Gd	0.55 Gd	5.0% Gd	1.6 Gd		
Gd-1	1.8% Gd	1.8% Gd	1 Gd	2.50% Gd	1.4 Gd	1.01% Gd	0.56 Mn^{2+}
Gd-2	0.17% Gd	0.15% Gd	0.88 Gd	0.24% Gd	1.4 Gd	0.47% Gd	2.7 Gd^{3+}
Mn-Gd-2	1.8% Mn	1.54% Mn	0.86 Mn	2.3% Mn	1.3 Mn		
	0.16% Gd	0.30% Gd	1.88 Gd	0.35% Gd	2.2 Gd		
Gd-3	35% Gd	7.5% Gd	0.22 Gd	10.1% Gd	0.29 Gd	7.20% Gd	0.21 Gd^{3+}

[a] Ion-exchange efficiencies above 1 are due to slight inhomogeneities in the suspension of trititanate nanotubes.

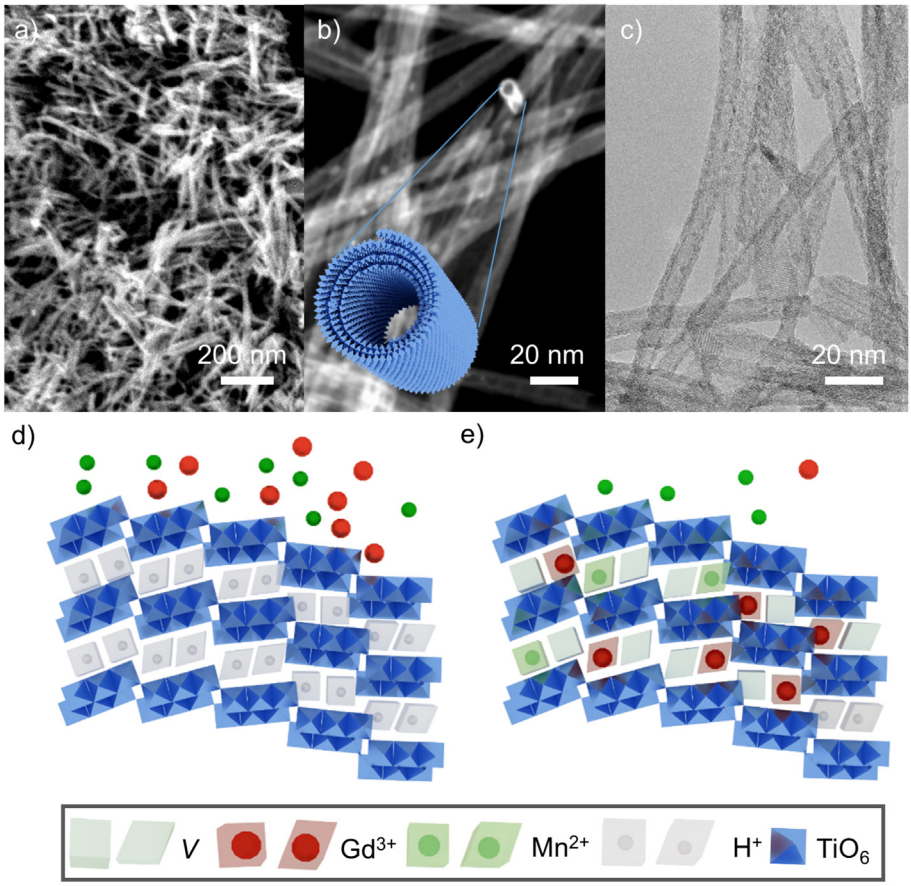

Fig. 1. a) SEM image of titanate nanotube powder. b) STEM image of the titanate nanotube powder. Inset shows the schematic view of the scroll-type trititanate nanotubes exhibiting the tubular structure with 3–4 layers. c) TEM image of titanate nanotubes. d)-e) Schematic of the wall segments of titanate nanotubes ion-exchanged with Mn^{2+} and Gd^{3+} ions. Red and green tetrahedra indicate the broad range of distorted sites for Gd^{3+} and Mn^{2+}. *V* stands for the vacancy sites formed due to the oxidation state differences. Note that ion-exchange with Gd^{3+} has higher affinity to ion-exchange positions as compared to Mn^{2+}. (For interpretation of the references to colour in this figure legend, the reader is referred to the web version of this article).

Gd-2, Mn-Gd-2, and Gd-3 were prepared by directly dissolving the salts ($Gd(CH_3CO_2)_3 \times H_2O$ for gadolinium and $Mn(NO_3)_2 \times H_2O$ for manganese ions) into the nanotube suspension.

Table 1 proves that ion-exchange is more efficient using the dissolved ionic salts, as Mn^{2+} doping efficiencies significantly increase with this method. From the results presented in Table 1 we observe that gadolinium is more favorably adsorbed into the trititanate nanotube structure compared to manganese at comparable nominal concentrations (Mn-1 and Gd-1 samples). This is further confirmed by the equally doped sample (Mn-Gd-1 sample), where the nominal concentrations are identical but the incorporated concentrations show a large disparity. This discrepancy is all the more spectacular given that the Gd^{3+} ions were introduced around 20 min later than the Mn^{2+} ions in this particular sample.

Both the observed ion-exchange equilibrium and the diffusion speed are shifted towards Gd^{3+} indicating that the intercalation capacity is larger and the ion-exchange kinetics is faster for this ion.

The faster ion-exchange for Gd^{3+} is in perfect agreement with the Nernst-Planck equations, which explain the different ion-exchange flux efficiencies as being a result of the slightly different electrochemical environment because of different oxidation states

and ionic sizes [46]. We believe that different atomic radii and oxidation states move the flux towards Gd^{3+} compared to Mn^{2+}. In theory, the atomic radius, r, is related to the efficiency of ionic exchange through the power law: $1/r^2$ [46]. This would suggest that the larger Gd^{3+} ions would have a slightly slower flux, however this might be compensated by its larger charge.

The preference for Gd^{3+} in the ion-exchange equilibrium can be explained in the framework of the hard and soft acids and bases theory (HSAB theory) [47,48], according to which soft bases, such as the host titanate structure react faster and stronger with soft acids. In our case, due to the large radius and high polarizability of Gd^{3+} as compared to Mn^{2+}, Gd^{3+} is a significantly *softer* acid, resulting in higher equilibrium intercalation [48].

3.2. ESR measurements

ESR is a microscopic, contactless method to study chemical environments and oxidation states of paramagnetic ions in crystal structures down to ppm level [49–55]. Using multi-frequency ESR, it is possible to provide more detailed microscopic information of the state, and to determine the effect of interactions [56–62].

Previous ESR studies revealed the role of Mn^{2+} and Gd^{3+} in nanocrystals and in glassy systems [44,45,63–65], but the effect of co-doping is less developed due to its complexity. Upon co-doping with these two different metal ions, the spin Hamiltonian describing the ESR spectra is

$$H{=}H(\mathrm{Mn}^{2+} - \mathrm{Gd}^{3+}) + H(\mathrm{Mn}^{2+}) + H(\mathrm{Gd}^{3+}) \quad (1)$$

where the first term is the interaction term between Mn^{2+} and Gd^{3+} ions. This unknown Hamiltonian might result in the relative change of dopant concentrations, and might dramatically modify the ESR spectra due to co-doping. The second and the third terms are the separate spin Hamiltonians for the two paramagnetic ions, which can be written in both cases as

$$H{=}H_Z + H_{SOC} + H_{ZFS} + H_{HF} \quad (2)$$

Here, the first term stands for the Zeeman interaction and the second is the spin-orbit coupling (SOC). The SOC dominates over the zero-field splitting (ZFS) in the rare earth materials but its sole effect is to select the pure spin state in Gd^{3+} as the lowest in the (L,S) manifold. The third term describes the ZFS due to the surrounding crystal electric fields, and the last term details the hyperfine coupling between the electron and nuclear spins.

Up to second order, the Hamiltonian of the zero-field splitting may be written as

$$H_{ZFS} = D(S_z^2 - S^2/3) + E(S_x^2 - S_y^2) \quad (3)$$

where D and E are the axial and rhombic zero-field splitting parameters, which describe the deviation from the octahedral and the axial symmetry [37,36].

Room-temperature X-band ESR, performed on the Mn-1, Gd-2 and Mn-Gd-2 samples, are shown in Fig. 2. In Ref. [33], we found that ESR spectra of Mn^{2+} doped scroll-type titanate nanotubes consist essentially of two components: i) a narrow sextet signal; and ii) a broad line with a linewidth of $\Delta B_{pp} = 48$ mT. The sextet component at $g = 2.001(4)$ with an $A_{iso} = 9.1$ mT hyperfine splitting is characteristic of Mn^{2+} in slightly distorted cubic sites (giving $2I+1$ lines for $I = 5/2$ nuclear spins). These non-cubic sites give rise to the coexistence of allowed ($\Delta m_I = 0$) and forbidden ($\Delta m_I = \pm 1$) transitions between the Zeeman sublevels of $m_S = \pm 1/2$ in the system with $S = 5/2$ electron spin. As in Ref. [33], we assume that the linewidth of these lines comes from the dipolar broadening. Our calculation based on Ref. [66] yields a distance between the Mn^{2+} ions of $d_{Mn\text{-}Mn} = 1.7(1)$ nm.

The broad component is superimposed with the narrow hyperfine sextet line with a linewidth of 5 times the $A_{iso} = 9.1$ mT hyperfine coupling. It originates from the non-central transitions ($m_S \neq \pm 1/2$) of the strongly distorted octahedral sites due to non-zero D and E zero-field splitting parameters. Similarly to polycrystalline systems, the strong angular dependence of these transitions results in an unresolvable component in our ESR spectra.

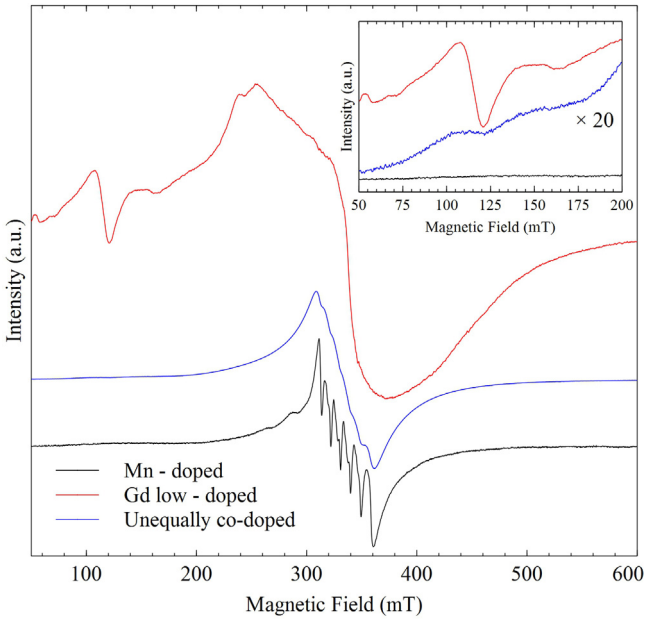

Fig. 2. X-Band ESR spectra of the Mn-1, Gd-2 and Mn-Gd-2 samples at room temperature. The Mn^{2+} sextet and broad signals clearly dominate in the $g = 2$ region. A higher scale view of the low-field part of the spectrum is given in the inset. The weak ESR signal components of the co-doped sample at low fields originate from the gadolinium doping.

In order to discern whether the ZFS estimated in doped titanate nanotubes stems only from the imperfect registry of TiO_6 octahedra or it comes from the large ion size that creates structural imperfections in the layered structure [67–69], we will calculate ZFS parameters in Gd^{3+} doped nanotubes.

The X-band ESR spectrum of the Gd-2 sample (see Fig. 2) is dominated by a broad feature stemming from strongly distorted sites. This is also known as the U spectrum, and it has already been explained for several polycrystalline and glassy systems (e.g., Gd^{3+} in soda-silica glass, or hydrated Na-Y zeolite) in Ref. [44] and in acyclic Gd(III) polyaminocarboxylates in Ref. [65]. Therein, the U spectrum was calculated as a sum of ESR spectra with a broad and unimodal distribution of zero-field splitting parameters. Below, we will discuss our multi-frequency ESR results using similar assumptions.

The low-field ESR spectrum of the unequally co-doped (Mn-Gd-2) sample in Fig. 2 is dominated by the ESR signal of Mn^{2+} around $g = 2$: one can resolve the characteristic manganese sextet with an $A_{iso} = 9.0(1)$ mT hyperfine splitting, corresponding to that reported in Ref. [33]. At low fields, however, we can identify the presence of the characteristic Gd^{3+} U spectrum. This is a direct confirmation of successful co-doping in our material. As above, the linewidth of the Mn^{2+} sextet lines are assigned to the dipolar broadening, which yields similar Mn^{2+} distances. This observation excludes that Gd^{3+} co-doping may force that Mn^{2+} ions occupy closer positions in the crystal lattice.

To further investigate effects and the sizes of ZFS parameters, we performed a multi-frequency ESR mapping of the presented materials at large microwave frequencies (52, 78, 105, 157, 210, 315, and 420 GHz). Fig. 3 shows the 315 GHz ESR spectra of the Mn-1, Gd-2 and Mn-Gd-2 samples. Whereas the ESR spectrum of the Mn-doped sample barely changes compared to the low-field

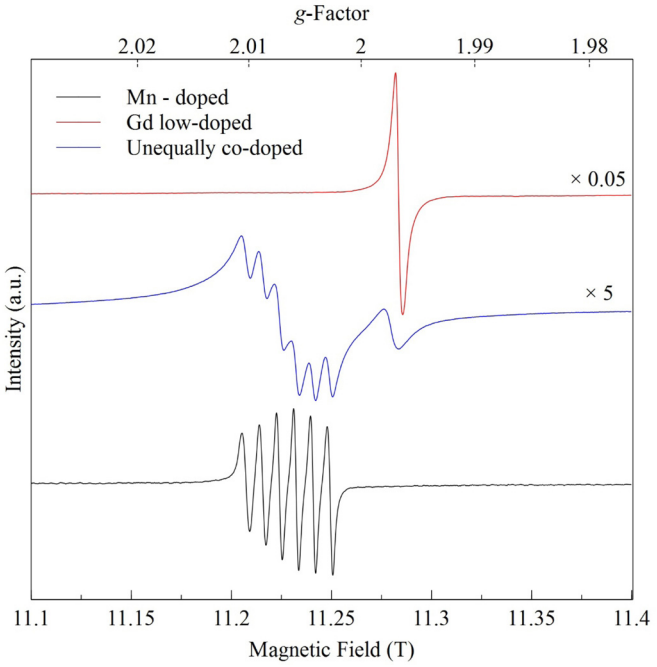

Fig. 3. High-field (315 GHz) ESR spectra of samples Mn-1, Mn-Gd-2 and Gd-2 at room temperature. Co-doping of manganese ions (Mn^{2+}) and gadolinium ions (Gd^{3+}), proven by the sextet signal at $g = 2.001(1)$, and the single derivative Lorentzian signal at $g = 1.995(1)$, is clearly visible.

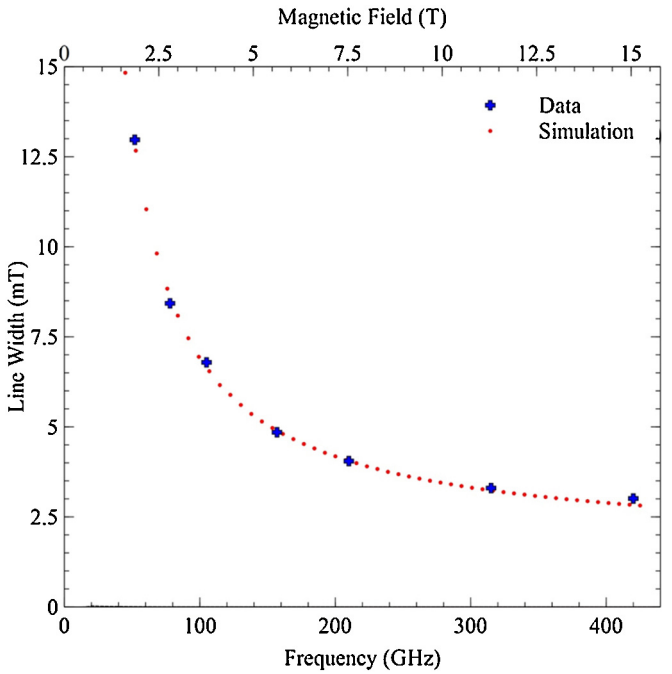

Fig. 4. ESR linewidth of the Gd-2 sample's ESR spectrum as a function of microwave frequency at room temperature. Red points correspond to simulated linewidths obtained from fitting of the zero-field splitting parameters. (For interpretation of the references to colour in this figure legend, the reader is referred to the web version of this article.)

case, a dramatic change is seen for the Gd^{3+}-doped samples. The complicated feature at low fields is replaced by a single, narrow, and symmetric ESR line at $g = 1.995(1)$.

This change of the line shape corresponds to a change in the ratio of ZFS parameters of Gd^{3+} as a function of the microwave frequency (magnetic field) [44]. In low fields, the H_{ZFS} term is larger than H_Z, hence, several transitions are observed within the Kramers levels, resulting in a complicated and broad ESR spectrum. In higher magnetic fields, the higher H_Z might overcome the strength of the zero-field splitting, and the transitions between the Zeeman sublevels start to dominate. In our nanomaterial, the observable single ESR line originates from transitions between the Zeeman sublevels of $m_S = \pm 1/2$. Transitions of Zeeman sublevels of $m_S \neq \pm 1/2$ are not resolvable in the background, as these are smeared out due to their angular dependence. The change of the ratio of the Zeeman and zero-field splitting energies can be followed by the ESR linewidth as a function of frequency (see Fig. 4).

Detailed analysis of the ESR spectrum of the Mn^{2+} ion-exchanged titanate nanotubes shows that the linewidth of the sextet components decreases, as well. In X-band, we found a linewidth of $\Delta B_{pp} = 9.0(1)$ mT, at 315 GHz it is $\Delta B_{pp} = 4.3(1)$ mT. This change, analogously to the case of Gd^{3+} ions, originates from a change of the ratio of Zeeman energy and zero-field splitting of Mn^{2+}. At high magnetic fields, we cannot observe the forbidden transitions of Mn^{2+} anymore, and the ESR linewidth is only a result of dipolar broadening.

Similarly to the low-field ESR spectrum, the presence of gadolinium ions is confirmed in the co-doped sample (Mn-Gd-2) by the outlying signal at $g = 1.995$. The ESR spectrum of the co-doped sample makes it possible to directly compare the intensities of the ESR lines stemming from Mn^{2+} (sextet lines and broad component) and from Gd^{3+} (single narrow line), yielding a measure of the absolute spin-susceptibility ratios: $\chi(Gd^{3+})/\chi(Mn^{2+}) = 0.6(1)\%$. This spin-susceptibility ratio is, however, in contradiction with EDX and XRF results which would suggest 15(5) % for the same ratio. The discrepancy is a further proof that a broad, unresolvable component is present in the high-field spectrum of Gd^{3+} ion intercalated titanate nanotubes. The spin-susceptibility of this component is much larger than that of the narrow ESR line.

In comparison with the singly intercalated gadolinium sample ($\Delta B_{pp} = 3$ mT) the line width of the gadolinium feature in the co-doped spectrum is significantly broader ($\Delta B_{pp} = 9$ mT). This difference can be explained by the slight differences in the ion-exchange efficiencies as confirmed by EDX and XRF studies (Table 1). In addition, it might point to the existence of interactions between neighboring manganese and gadolinium ions. The nature of these interactions remains undetermined but one significant possibility could be ferromagnetic interactions between the two ions, which are known to exist when isolated [70] but also in larger complexes [65].

Room-temperature frequency dependence of the ESR linewidth in the Gd-2 sample is shown in Fig. 4. As pointed out above, the narrowing of the ESR linewidth as a function of frequency is a result of the change of the ratio of the Zeeman and zero-field splitting energies.

In order to give a precise quantitative estimate of the ZFS parameters in titanate nanotubes, we simulated the ESR spectra following the *U* spectrum simulations of Ref. [44,45]. The Easyspin simulation calculates an $S = 7/2$ system using an isotropic $g = 1.995$ at room temperature for the Hamiltonian of Eq. (3). The ZFS parameters D and E were taken as an average of the values found in Ref. [45] for acyclic complexes. Furthermore, these values correspond to the range of values prescribed to the *U* spectrum ($0.051\ cm^{-1} \leq D \leq 0.056\ cm^{-1}$, $73\ mK \leq D \leq 80\ mK$, $1.5\ GHz \leq D \leq 1.7\ GHz$) given in Ref. [44].

To better simulate the broadening of the ESR spectrum, we assumed that the symmetry of ion-exchange positions in titanate nanotubes might differ from site to site leading to the variation of the ZFS parameters. Thus, we defined a Gaussian distribution around the central values of D and E that can quantify the magnitude of the variation of the ZFS parameters [45].

The widths of these Gaussian distributions, σ_D and σE, are fitted to the ESR linewidth data in Fig. 4. Furthermore, the intrinsic linewidth, ΔB_{int}, is a free, frequency-independent parameter. In Fig. 4, we show a fit to the linewidth data with the optimal fit parameters:

$$D = 0.054\,\mathrm{cm}^{-1} = 78\,\mathrm{mK} = 1.62\,\mathrm{GHz}, \sigma_D$$
$$= 0.30\,\mathrm{cm}^{-1} = 43\mathrm{mK} = 0.9\,\mathrm{GHz}$$

$$E = 0.015\,\mathrm{cm}^{-1} = 22\,\mathrm{mK} = 0.45\,\mathrm{GHz}, \sigma_E$$
$$= 0.064\,\mathrm{cm}^{-1} = 92\mathrm{mK} = 1.9\,\mathrm{GHz}$$

$$\Delta B_{int} = 6\,\mathrm{mT}$$

We notice that both for D and E, the standard deviation is a factor of 5 larger than the mean ZFS parameters. This can be explained by significant site-dependent distortions in the crystal structure around the rare earth metal ion.

Trititanate nanotubes possess scroll-type structure with diameters ranging from 7 to 10 nm [71]. Interestingly, the diameter distribution of these elongated tubular structures is relatively narrow as compared to other systems. The tube diameter is quite independent of synthesis conditions, the number of layers varies between 3 and 5 [69,71].

In these scroll-type titanate nanotubes [67], the significant spread of the ZFS parameters can be assigned to a change of curvature radii as a function of titanate layers (Fig. 1a). Therefore, calculation of the spread of zero-field splitting parameters is a measure of the curvature distribution. Hence, we predict that our technique could be used as a microscopic probe to study the layer number distribution of titanate nanotubes. As the thickness is only measurable locally using high-resolution microscopy techniques or X-ray diffraction, we suggest that such analysis (doping with ESR active cations combined with multi-frequency ESR study) might be of particular interest for diameter distribution analysis of large quantity of samples [69].

We assign the intrinsic linewidth, ΔB_{int} to dipolar broadening. In case of Gd^{3+} ($S = 7/2$), this linewidth points to a distance of $d_{Gd\text{-}Gd} = 1.9(1)$ nm, which is in good agreement with our homogeneous doping concentration.

We note that a similar study of the field dependence of the ESR linewidth could be performed in the case of Mn^{2+} substituted titanate nanotubes. However, the precision of the calculations would be limited by the weak frequency dependence. Therefore, Gd^{3+} would be better suited for the purpose of a diameter distribution analysis.

4. Conclusion

In conclusion, we synthesized homogeneous Mn^{2+} and Gd^{3+} co-doped titanate nanotubes through ionic exchange of scroll-type trititanate nanotubes prepared by the hydrothermal synthesis method. In comparison with Mn^{2+}, the saturation doping level of Gd^{3+} was found to be 3 times larger.

Our multi-frequency ESR studies complemented with detailed simulation of ESR spectra confirmed homogeneous distribution of the dopants in the rolled-up nanotubes, and found a significant spread of zero-field splitting parameters. It was found to originate from a large distribution of curvature radii. We suggest that our novel method based on the combination of ESR experiments and simulation could be also applied to characterize the distribution of the layer numbers in a trititanate nanotube sample.

Further tests are going on to compare the efficiency of other possible dopant atoms in $H_2Ti_3O_7$ nanotubes with special attention to more cost-efficient ions, such as Fe^{3+} and Cu^{2+}. Since calcination of titanate nanotubes and intercalated titanate nanotubes can yield the formation of titania nanotubes, nanorods and nanoparticles, better understanding of the rules of competitive ion-exchange processes in titanate nanotubes will potentially lead to the development of series of doped nano-titania having superior photocatalytic performance.

Competing interest

The authors declare no competing financial interest.

Acknowledgments

Fruitful discussions with András Jánossy are acknowledged. The work was supported by the Swiss National Science Foundation (Grant No. 200021_144419) and (Grant No. 670918). The authors wish to express their deepest and sincerest recognition of Prof. András Dombi a key figure in the topic of photocatalytic materials for the degradation of contaminants of environmental concern.

References

[1] K. Hashimoto, H. Irie, A. Fujishima, Jpn. J. Appl. Phys. 44 (12R) (2005) 8269.
[2] F.E. Osterloh, Chem. Mater. 20 (1) (2008) 35–54.
[3] B. O'Regan, M.1 Graetzel, Nature 353 (6346) (1991) 737–740.
[4] X. Chen, S.S. Mao, Chem. Rev. 107 (7) (2007) 2891–2959.
[5] K. Nakata, A. Fujishima, J. Photochem. Photobiol. C 13 (3) (2012) 169–189.
[6] A. Fujishima, X. Zhang, D. Tryk, Surf. Sci. Rep. 63 (12) (2008) 515–582.
[7] S. Malato, P. Fernández-Ibánez, M. Maldonado, J. Blanco, W. Gernjak, Catal. Today 147 (1) (2009) 1–59.
[8] M.M. Lee, J. Teuscher, T. Miyasaka, T.N. Murakami, H.J. Snaith, Science 338 (6107) (2012) 643–647.
[9] H.-S. Kim, C.-R. Lee, J.-H. Im, K.-B. Lee, T. Moehl, A. Marchioro, S.-J. Moon, R. Humphry-Baker, J.-H. Yum, J.E. Moser, et al., Sci. Rep. 2 (2012) 591.
[10] S.D. Stranks, G.E. Eperon, G. Grancini, C. Menelaou, M.J.P. Alcocer, T. Leijtens, L.M. Herz, A. Petrozza, H.J. Snaith, Science 342 (6156) (2013) 341–344.
[11] P.K. Dutta, A. Ginwalla, B. Hogg, B.R. Patton, B. Chwieroth, Z. Liang, P. Gouma, M. Mills, S. Akbar, J. Phys. Chem. B 103 (21) (1999) 4412–4422.
[12] M.M. Arafat, B. Dinan, S.A. Akbar, A.S.M.A. Haseeb, Sensors 12 (12) (2012) 7207–7258.
[13] D.B. Strukov, G.S. Snider, D.R. Stewart, R.S. Williams, Nature 453 (7191) (2008) 80–83.
[14] H. Wu, C. Xu, J. Xu, L. Lu, Z. Fan, X. Chen, Y. Song, D. Li, Nanotechnology 24 (45) (2013) 455401.
[15] M. Salari, K. Konstantinov, H.K. Liu, J. Mater. Chem. 21 (13) (2011) 5128.
[16] J. Xu, C. Jia, B. Cao, W. Zhang, Electrochim. Acta 52 (28) (2007) 8044–8047.
[17] K. Lee, A. Mazare, P. Schmuki, Chem. Rev. 114 (19) (2014) 9385–9454.
[18] F. Shao, J. Sun, L. Gao, S. Yang, J. Luo, J. Phys. Chem. C 115 (5) (2011) 1819–1823.
[19] Y. Ohsaki, N. Masaki, T. Kitamura, Y. Wada, T. Okamoto, T. Sekino, K. Niihara, S. Yanagida, Phys. Chem. Chem. Phys. 7 (24) (2005) 4157.
[20] N. Tétreault, E. Horváth, T. Moehl, J. Brillet, R. Smajda, S. Bungener, N. Cai, P. Wang, S.M. Zakeeruddin, L. Forró, A. Magrez, M. Grätzel, ACS Nano 4 (12) (2010) 7644–7650.
[21] T. Ohno, K. Sarukawa, K. Tokieda, M. Matsumura, J. Catal. 203 (1) (2001) 82–86.
[22] M. Wei, Y. Konishi, H. Zhou, H. Sugihara, H. Arakawa, J. Electrochem. Soc. 153 (6) (2006) A1232.
[23] G. Liu, N. Hoivik, K. Wang, Electrochem. Commun. 28 (2013) 107–110.
[24] N. Liu, K. Lee, P. Schmuki, Electrochem. Commun. 15 (1) (2012) 1–4.
[25] X. Chen, C. Burda, J. Am. Chem. Soc. 130 (15) (2008) 5018–5019.
[26] H. Liu, G. Liu, G. Xie, M. Zhang, Z. Hou, Z. He, Appl. Surf. Sci. 257 (8) (2011) 3728–3732.
[27] J. Yu, Q. Xiang, M. Zhou, Appl. Catal. B Environ. 90 (3) (2009) 595–602.
[28] R.-A. Doong, S.-M. Chang, C.-W. Tsai, Appl. Catal. B Environ. 129 (2013) 48–55.
[29] X. Zhao, Z. Cai, T. Wang, S. O'Reilly, W. Liu, D. Zhao, Appl. Catal. B Environ. 187 (2016) 134–143.
[30] T. Kasuga, M. Hiramatsu, A. Hoson, T. Sekino, K. Niihara, Langmuir 14 (12) (1998) 3160–3163.
[31] W. Zhao, X. Wang, H. Sang, K. Wang, Chin. J. Chem. 31 (3) (2013) 415–420.
[32] P. Dong, Y. Wang, B. Liu, L. Guo, Y. Huang, S. Yin, J. Am. Ceram. Soc. 95 (1) (2011) 82–84.
[33] P. Szirmai, E. Horváth, B. Náfrádi, Z. Micković, R. Smajda, D.M. Djokić, K. Schenk, L. Forró, A. Magrez, J. Phys. Chem. C 117 (1) (2013) 697–702.
[34] J. Coey, Curr. Opin. Solid State Mater. Sci. 10 (2) (2006) 83–92.

[35] T. Nakajima, L.R. Sheppard, K.E. Prince, J. Nowotny, T. Ogawa, Adv. Appl. Ceram. 106 (1–2) (2007) 82–88.
[36] F. Simon, A. Rockenbauer, T. Fehér, A. Jánossy, C. Chen, A.J.S. Chowdhury, J.W. Hodby, Phys. Rev. B 59 (18) (1999) 12072–12077.
[37] A. Jánossy, F. Simon, T. Fehér, A. Rockenbauer, L. Korecz, C. Chen, A.J.S. Chowdhury, J.W. Hodby, Phys. Rev. B 59 (2) (1999) 1176–1184.
[38] E. Horváth, I. Szilágyi, L. Forró, A. Magrez, J. Colloid Interface Sci. 416 (2014) 190–197.
[39] D.V. Bavykin, J.M. Friedrich, A.A. Lapkin, F.C. Walsh, Chem. Mater. 18 (5) (2006) 1124–1129.
[40] B. Náfrádi, R. Gaál, T. Fehér, L. Forró, J. Magn. Reson. 192 (2) (2008) 265–268.
[41] B. Náfrádi, R. Gaál, A. Sienkiewicz, T. Fehér, L. Forró, J. Magn. Reson. 195 (2) (2008) 206–210.
[42] P. Szirmai, G. Fábián, B. Dóra, J. Koltai, V. Zólyomi, J. Kürti, N.M. Nemes, L. Forró, F. Simon, Phys. Status Solidi B 248 (11) (2011) 2688–2691.
[43] S. Stoll, A. Schweiger, J. Magn. Reson. 178 (1) (2006) 42–55.
[44] C.M. Brodbeck, L.E. Iton, J. Chem. Phys. 83 (9) (1985) 4285.
[45] M. Benmelouka, J. Van Tol, A. Borel, M. Port, L. Helm, L.C. Brunel, A.E. Merbach, J. Am. Chem. Soc. 128 (24) (2006) 7807–7816.
[46] F. Helfferich, Ion Exchange, Dover, Courier Corporation (1962).
[47] R.G. Pearson, J. Am. Chem. Soc. 85 (22) (1963) 3533–3539.
[48] R.G. Pearson, J. Chem. Educ. 64 (7) (1987) 561.
[49] J. Jaćimović, E. Horváth, B. Náfrádi, R. Gaál, N. Nikseresht, H. Berger, L. Forró, A. Magrez, Appl. Phys. Lett. Mater. 1 (3) (2013) 1–7.
[50] P. Szirmai, G. Fábián, J. Koltai, B. Náfrádi, L. Forró, T. Pichler, O.A. Williams, S. Mandal, C. Bäuerle, F. Simon, Phys. Rev. B 87 (2013) 195132.
[51] P. Szirmai, B. Náfrádi, A. Arakcheeva, E. Szilágyi, R. Gaál, N.M. Nemes, X. Berdat, M. Spina, L. Bernard, J. Jaćimović, A. Magrez, L. Forró, E. Horváth, Catal. Today 284 (2017) 52–58, http://dx.doi.org/10.1016/j.cattod.2016.10.024.
[52] B. Náfrádi, N.M. Nemes, T. Fehér, L. Forró, Y. Kim, J.E. Fischer, D.E. Luzzi, F. Simon, H. Kuzmany, Phys. Status Solidi B 243 (13) (2006) 3106–3110.
[53] L. Ćirić, K. Pierzchala, A. Sienkiewicz, A. Magrez, B. Náfrádi, D. Alexander, J. Warner, H. Shinohara, M.H. Ruemmeli, T. Pichler, et al., Phys. Status Solidi B 245 (10) (2008) 2042–2046.
[54] Y. Lakhdar, C. Mézière, L. Zorina, M. Giffard, P. Batail, E. Canadell, P. Auban-Senzier, C. Pasquier, D. Jérome, B. Náfrádi, et al., J. Mater. Chem. 21 (5) (2011) 1516.
[55] B. Náfrádi, L. Forró, M. Choucair, Phys. Status Solidi B 251 (12) (2014) 2521–2524.
[56] B. Náfrádi, M. Choucair, L. Forró, Carbon 74 (0) (2014) 346–351.
[57] Á. Antal, T. Fehér, B. Náfrádi, R. Gaál, L. Forró, A. Jánossy, Physica B 405 (11, Supplement) (2010) S168–S171.
[58] Á. Antal, T. Fehér, E. Tátrai-Szekeres, F. Fülöp, B. Náfrádi, L. Forró, A. Jánossy, Phys. Rev. B 84 (*2011*) 075124.
[59] Á. Antal, T. Fehér, B. Náfrádi, L. Forró, A. Jánossy, Phys. Status Solidi B 249 (5) (2012) 1004–1007.
[60] B. Náfrádi, Á. Antal, Á. Pásztor, L. Forró, L. Kiss, T. Fehér, E. Kováts, S. Pekker, A. Jánossy, J. Phys. Chem. Lett. 3 (22) (2012) 3291–3296.
[61] B. Náfrádi, M. Choucair, P.D. Southon, C.J. Kepert, L. Forró, Chem. Eur. J. 21 (2) (2014) 770–777.
[62] K. Nagy, B. Náfrádi, N. Kushch, E. Yagubskii, E. Herdtweck, T. Fehér, L. Kiss, L. Forró, A. Jánossy, Phys. Rev. B 80 (10) (2009).
[63] B.T. Allen, J. Chem. Phys. 43 (11) (1965) 3820.
[64] S.K. Misra, Physica B 203 (1–2) (1994) 193–200.
[65] T.K. Prasad, M.V. Rajasekharan, J.-P. Costes, Angew. Chem. Int. Ed. 46 (16) (2007) 2851–2854.
[66] J.H. Van Vleck, Phys. Rev. 74 (9) (1948) 1168–1183.
[67] A. Kukovecz, M. Hodos, E. Horváth, G. Radnóczi, Z. Kónya, I. Kiricsi, J. Phys. Chem. B 109 (38) (2005) 17781–17783.
[68] M. Gateshki, Q. Chen, L.-M. Peng, P. Chupas, V. Petkov, Z. Kristallogr. (2007), 222(11/2007).
[69] D. Bavykin, F. Walsh, Titanate and titania nanotubes: synthesis, properties and applications, R. Soc. Chem. (RSC) (2009).
[70] J.-P. Costes, J.-P. Tuchagues, L. Vendier, J. Garcia-Tojal, Eur. J. Inorg. Chem. 2013 (19) (2013) 3307–3311.
[71] Y. Mao, S.S. Wong, J. Am. Chem. Soc. 128 (25) (2006) 8217–8226.